Materials Today Bio 32 (2025) 101696

Contents lists available at ScienceDirect

Materials Today Bio

journal homepage: www.journals.elsevier.com/materials-today-bio

A triple-mode strategy on JQ1-loaded nanoplatform for superior antitumor therapy in pancreatic cancer

Zhiguo Li [a,1], Jinxin Duan [a,1], Zhiwen Liu [b,1], Weifan Li [a,1], Yiyin Mai [a], Hao Fu [a,*], Guotao Yuan [c,e,**], Jiawei Wang [a,d,***]

[a] Guangzhou Key Laboratory of Medical Nanomaterials, Guangdong Provincial Key Laboratory of Malignant Tumor Epigenetics and Gene Regulation, Guangdong-Hong Kong Joint Laboratory for RNA Medicine, Medical Research Center, Sun Yat-sen Memorial Hospital, Sun Yat-sen University, Guangzhou, 510120, China
[b] School of Life Sciences and Biopharmaceutics, Guangdong Pharmaceutical University, Guangzhou, 510006, China
[c] College of Chemistry and Environmental Engineering, Shenzhen University, 518060, China
[d] Breast Tumor Center, Sun Yat-sen Memorial Hospital, Sun Yat-sen University, Guangzhou, 510120, China
[e] Department of Otolaryngology, Longgang E.N.T. Hospital & Shenzhen Key Laboratory of E.N.T., Shenzhen, 518116, China

ARTICLE INFO

Keywords:
Pancreatic cancer
Tumor microenvironment
Bromodomain
Ferroptosis
Immunogenic cell death

ABSTRACT

Pancreatic cancer's dire prognosis urgently calls for innovative therapeutic strategies. JQ1, a bromodomain 4 inhibitor, exhibits potent anti-tumor activity in preclinical models but faces limitations due to rapid resistance development. Here, we developed a novel multifunctional nanoplatform, JQ1@MSN/FeTA-iRGD, which implemented a triple-mode strategy integrating apoptosis, ferroptosis, and immunogenic cell death for optimized treatment of pancreatic cancer. The particles could precisely target tumors in mice and achieve efficient release of JQ1 and Fe^{2+} through internalization in the acidic tumor environment. The nanoplatform amplified reactive oxygen species and mitochondrial damage to disrupt the redox homeostasis, thus synergistically escalating apoptosis and ferroptosis for the destruction of tumor cells, circumventing the rapid drug resistance associated with monotherapy. Meanwhile, dying cancer cells released damage-associated molecular patterns, which facilitated immunogenic cell death and triggered antitumor immune responses, guaranteeing the sustained efficacy of the treatment. Moreover, the system exhibited favorable biocompatibility, supporting its feasibility for clinical translation. Our results demonstrated that this novel strategy, combining apoptosis, ferroptosis, and immunogenic cell death, overcame the limitations of monotherapy with JQ1, providing a superior, targeted, and sustainable treatment option for pancreatic cancer.

1. Introduction

Pancreatic cancer, with a five-year survival rate of only 5–12 % [1,2], is the third leading cause of cancer-related deaths worldwide, posing a major challenge to international health initiatives [2–4]. It is concerning that pancreatic cancer patients often exhibit poor responses to chemotherapy [5], with a median survival of just 11 months under first-line treatments [6], highlighting the urgent need for more effective therapeutic strategies for this patient population [7]. Studies have identified bromodomain 4 (BRD4), an acetyl-lysine binding protein crucial for oncogene regulation and epigenetic modifications, as a promising cancer therapy target [8]. Inhibiting BRD4 disrupts RNA polymerase II-driven transcription, selectively targeting essential oncogenes for cancer cell survival [9–11]. JQ1, one of the initial bromodomain and extraterminal domain (BET) inhibitors identified, disrupts the association between BET proteins and acetylated lysines on histones and

* Corresponding author. Guangzhou Key Laboratory of Medical Nanomaterials, Guangdong Provincial Key Laboratory of Malignant Tumor Epigenetics and Gene Regulation, Guangdong-Hong Kong Joint Laboratory for RNA Medicine, Medical Research Center, Sun Yat-sen Memorial Hospital, Sun Yat-sen University, Guangzhou, 510120, China.
** Corresponding author. College of Chemistry and Environmental Engineering, Shenzhen University, 518060, China.
*** Corresponding author. Guangzhou Key Laboratory of Medical Nanomaterials, Guangdong Provincial Key Laboratory of Malignant Tumor Epigenetics and Gene Regulation, Guangdong-Hong Kong Joint Laboratory for RNA Medicine, Medical Research Center, Breast Tumor Center, Sun Yat-sen Memorial Hospital, Sun Yat-sen University, Guangzhou, 510120, China.
E-mail addresses: fuhao28@mail.sysu.edu.cn (H. Fu), yuanguotao2942@163.com (G. Yuan), wangjw32@mail2.sysu.edu.cn (J. Wang).
[1] These authors contribute equally.

https://doi.org/10.1016/j.mtbio.2025.101696
Received 28 November 2024; Received in revised form 11 March 2025; Accepted 20 March 2025
Available online 21 March 2025

transcription factors, inhibiting oncogene expression [12]. JQ1 shows promising anti-proliferative and pro-apoptotic effects in various tumors, including multiple myeloma, acute myeloid leukemia, triple-negative breast cancer, pancreatic cancer, and NUT midline carcinoma, consequently positioning it as an innovative epigenetic therapy for multiple cancer types [13–17]. Although JQ1 has shown strong anti-tumor effects in various preclinical cancer models, its long-term efficacy is hindered by the rapid development of resistance through mechanisms like increased autophagy, and adaptive pathway activation [16,18–20]. To achieve sustained therapeutic effects, JQ1 typically needs to be combined with therapies targeting complementary pathways.

Ferroptosis, an iron-dependent form of programmed cell death, differs notably from apoptosis, pyroptosis, and autophagy [21]. The core of ferroptosis is the elevation of labile intracellular iron, which drives the Fenton reaction, transforming hydrogen peroxide (H_2O_2) into highly toxic hydroxyl radicals (•OH) [22]. This reaction leads to reactive oxygen species (ROS) production, inducing lipid peroxidation and cell membrane damage, culminating in cell death [23]. Ferroptosis has emerged as a promising cancer therapy strategy because it directly kills tumor cells independently of apoptotic effectors and necrosis inducers, offering potential to overcome treatment resistance [24,25]. Furthermore, ferroptosis induces immunogenic cell death (ICD), enhancing tumor-specific immunity. Tumor cell ferroptosis can release damage-associated molecular patterns (DAMPs), such as the externalization of calreticulin (CRT) and the secretion of adenosine triphosphate (ATP), which subsequently recruit immune cells to infiltrate the tumor, promoting their activation, differentiation and maturation, ultimately inducing tumor-specific cytotoxicity [26]. Thus, we suggest an organic combination of JQ1 and ferroptosis to mitigate the rapid resistance caused by JQ1 monotherapy, while achieving long-term effectiveness by triggering an immune response, thereby addressing limitations of JQ1's short-lived efficacy.

Therefore, we developed a novel multifunctional nanoplatform, JQ1@MSN/FeTA-iRGD, specifically designed to enhance pancreatic cancer therapy by adopting a triple-mode strategy integrating apoptosis, ferroptosis, and ICD (Scheme 1). As illustrated, mesoporous silica nanoparticles (MSN) offered excellent JQ1 loading capacity owing to their high specific surface area. The metal-organic-frameworks (MOF) shell, formed by the coordination of Fe^{2+} and tannic acid (TA), effectively promoted the Fenton reaction, while the conjugation of iRGD ensured precise targeting of the pancreatic cancer [27–29]. In the tumor's acidic environment, protonation of the phenolic hydroxyl groups in TA disrupted the FeTA complex, triggering the release of JQ1 and Fe^{2+}. JQ1, as a BRD4 inhibitor, inhibited tumor cell proliferation, damaged mitochondria, and promoted ROS production, disrupting the tumor cells' redox balance and inducing apoptosis. Subsequently, the generated Fe^{2+} exacerbated ROS production via the Fenton reaction, causing lipid peroxidation and ferroptosis, which synergized with apoptosis to amplify the anticancer effects. Furthermore, dying tumor cells triggered ICD and stimulated a tumor-specific immune response, effectuating a triple-mode strategy for tumor suppression.

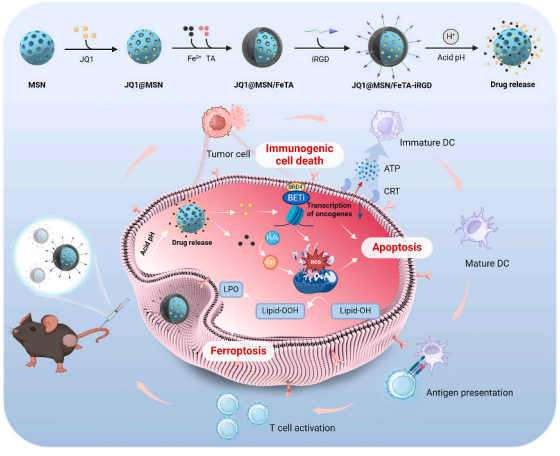

Scheme 1. Diagram of the preparation and mechanism of action of JQ1@MSN/FeTA-iRGD.

2. Results and discussion

2.1. Synthesis and characterization

The preparation of JQ1@MSN/FeTA-iRGD is described as Scheme 1. Briefly, MSN was stirred with JQ1 in water for loading, followed by coating a FeTA layer and modifying the surface with iRGD to fabricate JQ1@MSN/FeTA-iRGD. The morphology of JQ1@MSN/FeTA-iRGD was characterized by transmission electron microscopy (TEM). JQ1@MSN/FeTA shows the mesoporous structure enveloped by the FeTA layer (Fig. 1A). Dynamic light scattering analysis (Fig. 1B) shows that the JQ1@MSN/FeTA have an average hydrodynamic size of 55 nm, slightly larger than that of MSN, which helps prolong their circulation time in the body. Zeta potential analysis (Fig. S1) shows that JQ1@MSN/FeTA has a negative charge, which helps avoid clearance by *in vivo* immune response. Subsequently, X-ray diffraction (XRD) spectrum was presented to reveal the characteristics of their crystalline structure. The XRD spectrum of JQ1@MSN/FeTA (Fig. 1C) shows a broad diffraction peak at 22° similar to silica, with no other structures detected. The FTIR spectrum (Fig. 1D) of JQ1@MSN/FeTA-iRGD nanoparticles shows the features similar to those of JQ1 and RGD, indicating successful surface loading of these components. X-ray photoelectron spectroscopy (XPS) survey spectrum (Fig. 1E, F, S2) of JQ1@MSN/FeTA-iRGD reveals Fe-modified chemical state andverifing the successful synthesis of JQ1@MSN/FeTA-iRGD nanoparticles.

Furthermore, the JQ1-loaded efficiency of JQ1@MSN/FeTA nanoparticles was evaluated. By varying the weight ratio of JQ1 to MSN/FeTA carrier, the loading efficiency of JQ1increases along with the ratio, reaching a saturation loading efficiency of 21.7 % at a ratio of 5 (JQ1: MSN/FeTA, w/w) (Figs. S3 and S4).

The Brunauer-Emmett-Teller results (Fig. 1G) show that the mesopore size of MSN is 11.28 nm, indicating its suitability as a drug carrier. The JQ1@MSN/FeTA NPs were composed of the elements silicon (Si), oxygen (O) and iron (Fe), with a homogeneous distribution (Fig. S5). The Fe content in JQ1@MSN/FeTA NPs was measured to be 4.9 % by ICP-MS. Furthermore, the JQ1-released behavior of JQ1@MSN/FeTA nanoparticles was investigated under simulated physiological and tumor microenvironment conditions at different pH levels (pH 7.4, 6.5, and 5.5). The results showed that the release ratio of JQ1 exhibited significant pH-dependency, with the fastest release at pH 5.5 and the slowest at pH 7.4 (Fig. 1H). Additionally, through inductively coupled plasma mass spectrometry (ICP-MS) analysis of Fe cumulative release, we confirmed that the release pattern of Fe was similar to that of JQ1 (Fig. 1I). The release curves of JQ1@MSN/FeTA nanoparticles under these conditions displayed high correlation coefficients, indicating high predictability and reproducibility of the release behavior. These findings indicate the tremendous potential of JQ1@MSN/FeTA nanoparticles as pH-responsive delivery systems, particularly in cancer therapy, where they can rapidly release drugs under the acidic conditions of the tumor microenvironment, thereby enhancing therapeutic effects and reducing damage to normal cells. Additionally, JQ1@MSN/FeTA remained stable for over seven days in various physiological environments (PBS, serum, DMEM solution), demonstrating potential for further biomedical applications (Fig. S6).

2.2. JQ1@MSN/FeTA promotes both apoptosis and ferroptosis in tumor cells, exhibiting significant antitumor activity in vitro

Initial *in vitro* investigations assessed the antitumor efficacy of

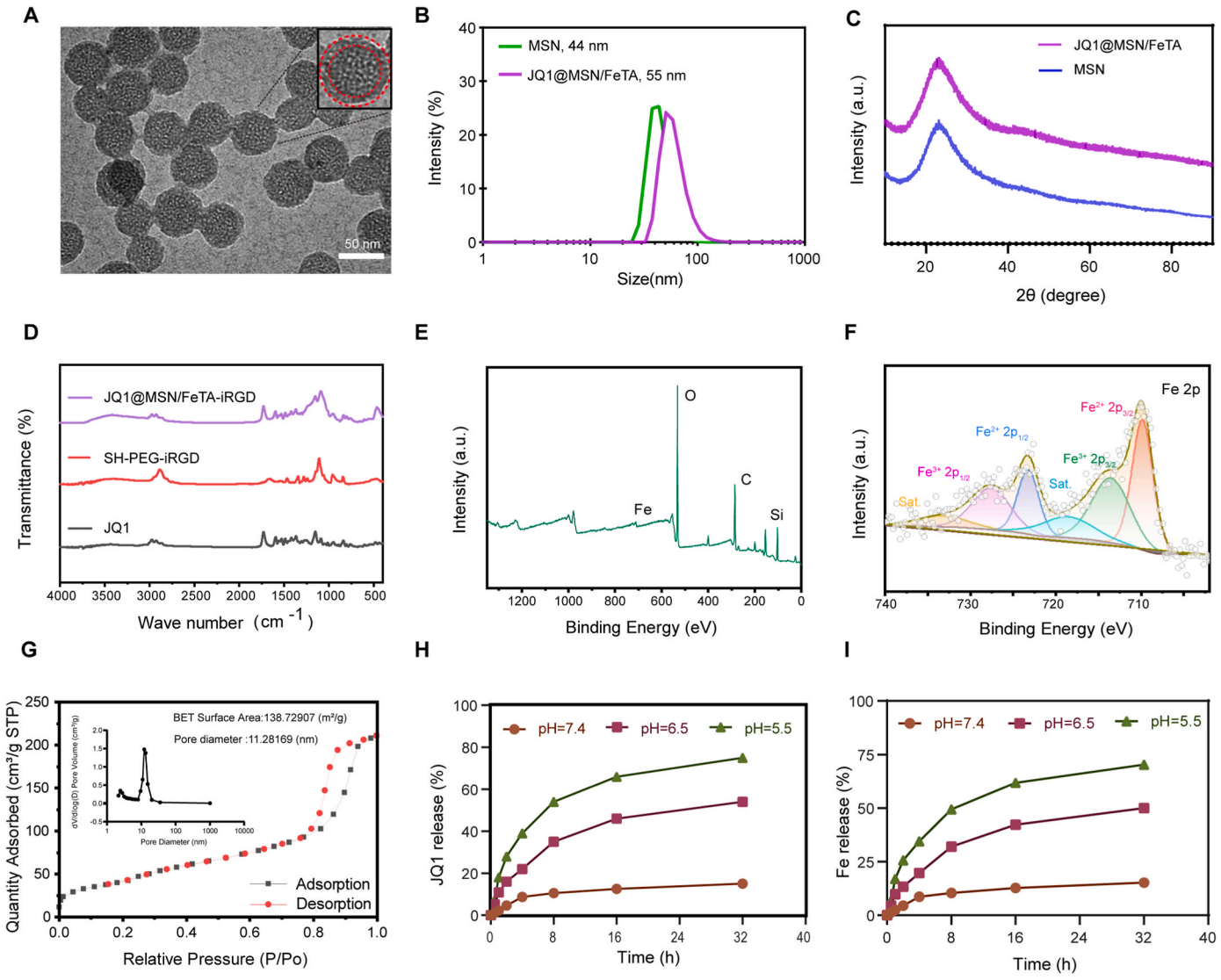

Fig. 1. Synthesis and characterization of JQ1@MSN/FeTA-iRGD. A. TEM images of JQ1@MSN/FeTA NPs. B. Dynamic light scattering. C. X-ray diffraction (XRD) patterns. D. FTIR spectra of JQ1、SH-PEG-iRGD and JQ1@MSN/FeTA-iRGD. E, F. X-ray photoelectron spectroscopy (XPS) scans of JQ1@MSN/FeTA, Fe 2p shifts and an XPS survey spectrum. G. N_2 adsorption/desorption isotherms of MSN. Insets are their corresponding pore size distributions. H. JQ1 release profiles from JQ 1@MSN/FeTA at different pH values *in vitro*. I. *In vitro* cumulative release of ferric ions from JQ1@MSN/FeTA.

JQ1@MSN/FeTA. A CCK-8 assay was conducted to evaluate the effects of various concentrations of the compound on Panc02 cell viability. The MSN/FeTA group showed low toxicity, while the JQ1@MSN/FeTA group exhibited significantly higher antitumor activity than the JQ1 group (Fig. 2A–S7). Subsequent validation across multiple cell lines confirmed the therapeutic effects of JQ1@MSN/FeTA (Fig. 2B), with IC50 values ranging from 82.79 to 129.76 μg/ml (Fig. S8). Consistent with the CCK-8 results, Calcein-AM and PI dual staining confirmed the potent cytotoxic effects of JQ1@MSN/FeT A (Fig. 2C–S9). Colony formation assays further highlighted JQ1@MSN/FeTA's potential to inhibit tumor cell proliferation (Fig. 2D).

In subsequent experiments, we employed 2′,7′-dichlorofluorescin diacetate to evaluate ROS generation. Fluorescence microscopy revealed a modest increase in ROS levels in the JQ1 group, whereas ROS production in the JQ1@MSN/FeTA group was significantly enhanced (Fig. 2E–S10). This trend was confirmed by flow cytometry (Fig. S11). This suggests that JQ1@MSN/FeTA significantly boosts ROS production via the synergistic action of Fe release and JQ1. Lipid peroxidation, a hallmark of ferroptosis, was measured using flow cytometry, revealing significantly higher levels in the JQ1@MSN/FeTA group (Fig. 2F). Glutathione peroxidase 4 (GPX4) inactivation was considered a necessary factor promoting lipid peroxidation during ferroptosis. Western blot analysis revealed that the expression of GPX4 in the JQ1@MSN/FeTA group was significantly lower than that in the control group, indicating that JQ1@MSN/FeTA promoted lipid peroxide accumulation by suppressing GPX4 activity (Fig. 2G). Mitochondria plays a central role in cellular oxidative stress and regulate ferroptosis through multiple pathways [30]. Mitochondrial membrane potential, assessed using the JC-1 probe, showed a significant decrease in red fluorescence in the JQ1 group, indicating mitochondrial impairment. In contrast, increased green fluorescence in the JQ1@MSN/FeTA group suggested more severe mitochondrial damage (Fig. 2H–S12). Further, Annexin V and PI dual staining showed that the apoptosis rate in the JQ1@MSN/FeTA group (61.9 %) was markedly higher than in the JQ1 group (25.6 %), underscoring the potent apoptotic effects of JQ1@MSN/FeTA (Fig. 2I).

2.3. *JQ1@MSN/FeTA induces ICD, promoting maturation of dendritic cells (DCs) in vitro*

Ferroptotic tumor cells release DAMPs, triggering ICD and

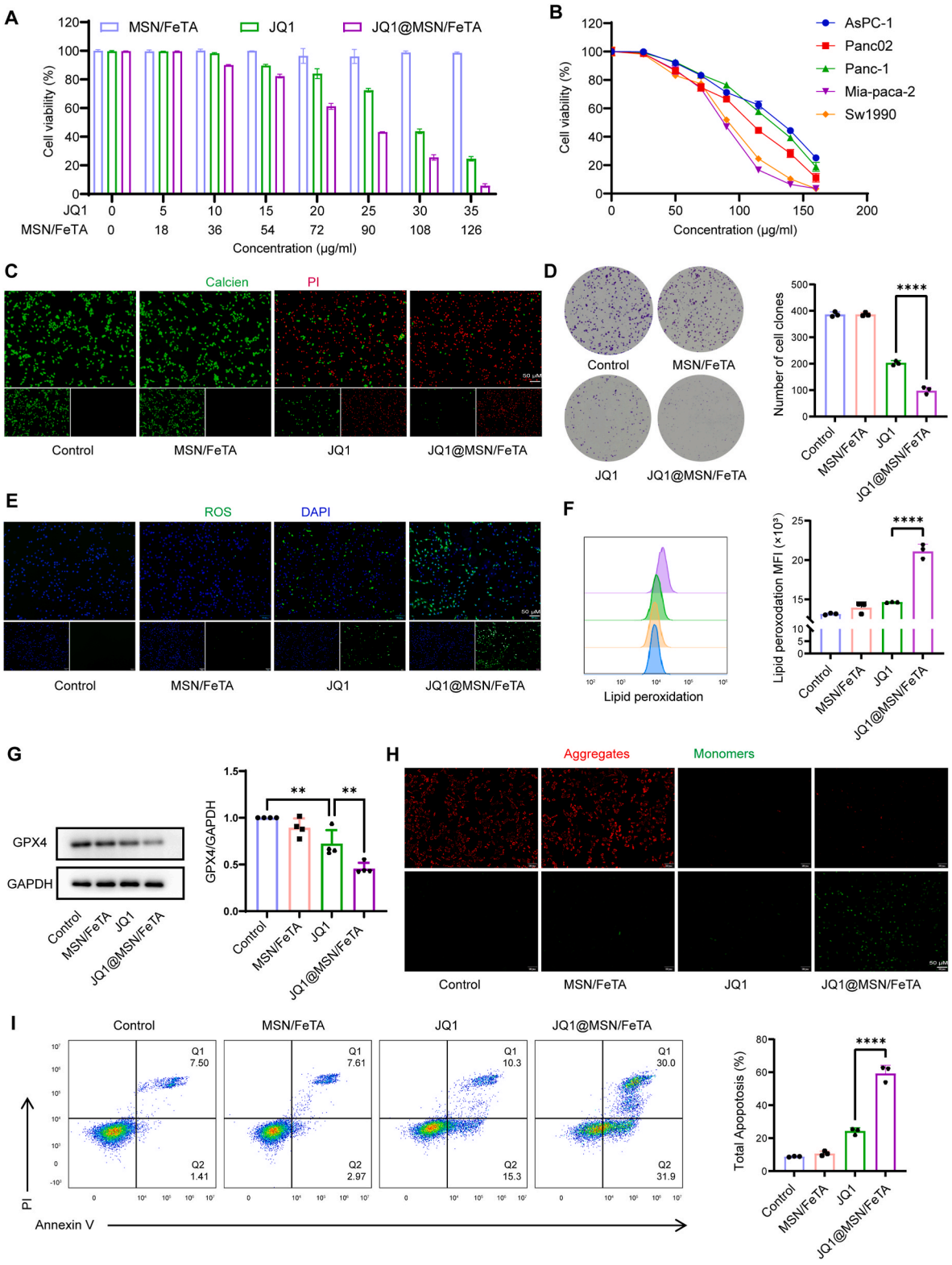

Fig. 2. JQ1@MSN/FeTA promotes both apoptosis and ferroptosis in tumor cells, exhibiting significant antitumor activity in vitro. A. Viabilities of Panc02 cells after 24 h of treatment with MSN/FeTA, JQ1, JQ1@MSN/FeTA. B. Viabilities of various pancreatic cancer cell lines after 24 h of treatment with JQ1@MSN/FeTA. C. Fluorescence microscopy images of Calcein/PI staining of Panc02 cells after 24 h of treatment with PBS, MSN/FeTA, JQ1, and JQ1@MSN/FeTA. D. Colony formation images and quantitative analysis of Panc02 cells treated with different compounds. E. Fluorescence images of ROS detection after incubating Panc02 cells with different compounds for 12 h. F. Flow cytometry analysis of Lipid Peroxidation Detection. G. Western blot analysis of GPX4 protein expression. H. Fluorescence images of mitochondrial membrane potential. I. Apoptosis analysis of Panc02 cells treated with different compounds for 12 h, assessed by flow cytometry.

generating tumor-specific immune responses. We focused on three key ICD markers: ROS production, CRT exposure, and ATP secretion. Previous results demonstrated that the JQ1@MSN/FeTA group generated significantly higher levels of ROS compared to the JQ1 monotherapy and MSN/FeTA groups. ATP levels in cell culture supernatants, measured with a commercial ATP assay kit, showed a significant increase in the JQ1@MSN/FeTA group (Fig. 3A). Flow cytometry analysis revealed significantly enhanced levels of CRT in the JQ1@MSN/FeTA group (Fig. 3B). To assess the impact of ferroptotic tumor cells on DCs maturation, Panc02 cells treated with nanomaterials were co-cultured with bone marrow-derived dendritic cells (BMDCs) in a transwell system for 48 h. Subsequently, DCs were collected, and co-expression of co-stimulatory molecules CD80 and CD86 was analyzed by flow cytometry (Fig. 3C). Results indicated that JQ1@MSN/FeTA treatment significantly promoted DCs maturation ($CD80^+$ $CD86^+$) (Fig. 3D). Supernatants were collected from cultured DCs for the measurement of pro-inflammatory cytokine levels using ELISA. As shown in Fig. 3F, the secretion of IL-1β, IL-6, IL-12p60, and TNF-α by BMDCs was significantly increased in the experimental group. Additionally, $CD8^+$ T cells co-cultured with activated BMDCs showed that JQ1@MSN/FeTA treatment significantly enhanced T cell proliferation (Fig. 3E–I). These findings suggest that ferroptotic tumor cells, induced by JQ1@MSN/FeTA, effectively promote BMDCs maturation and subsequent T cell activation.

2.4. JQ1@MSN/FeTA-iRGD demonstrates excellent tumor-targeting capabilities

iRGD is a targeting peptide composed of nine amino acids that enhances drug uptake by tumor cells, increases drug accumulation at tumor sites, and facilitates deeper penetration of drugs into pancreatic tumors [26–28]. To enhance tumor-targeting capabilities, the JQ1@MSN/FeTA nanoparticles were functionalized with iRGD. Initially, tumor cell uptake of these nanomaterials was evaluated *in vitro* using flow cytometry (Fig. 4A), showing that the uptake of Cy5.5-JQ1@MSN/FeTA-iRGD was significantly enhanced compared to Cy5.5-JQ1@MSN/FeTA. Confocal microscopy images at 8 h post-treatment clearly showed enhanced uptake by tumor cells in the iRGD group (Fig. 4B). Subsequently, the Cy5.5-JQ1@MSN/FeTA-iRGD nanoparticles were intravenously administered to C57BL/6 mice with subcutaneous Panc02 tumors, with animal imaging used to monitor enrichment of these nanoparticle in the tumors. Compared to Cy5.5-JQ1@MSN/FeTA, Cy5.5-JQ1@MSN/FeTA-iRGD showed more distinct and concentrated accumulation at the tumor site, peaking at 12 h (Fig. 4C). These findings were confirmed by subsequent organ fluorescence imaging (Fig. 4D). This biodistribution highlights the role of iRGD modification in enhancing tumor-specific delivery and retention of therapeutic nanoparticles, potentially reducing systemic toxicity and improving therapeutic outcomes.

2.5. Antitumor effects of JQ1@MSN/FeTA-iRGD in vivo

JQ1@MSN/FeTA-iRGD effectively induced ferroptosis and ICD in tumor cells *in vitro*, while also demonstrating excellent tumor accumulation *in vivo*. We evaluated the *in vivo* antitumor activity of JQ1@MSN/FeTA-iRGD using a subcutaneous Panc02 mouse model. A pancreatic cancer model was established by subcutaneously injecting Panc02 cells. Upon reaching a tumor volume of 50 mm^3, the mice were divided into five groups with equal tumor sizes and treatment groups were received daily drug administration for five consecutive days (Fig. 5A). Fig. 5B shows no significant changes in body weight across treatment groups. Tumor sizes increased gradually in the PBS and MSN/FeTA groups, whereas JQ1 monotherapy slowed tumor growth. As expected, the JQ1@MSN/FeTA and JQ1@MSN/FeTA-iRGD groups displayed strong antitumor effects, particularly in the JQ1@MSN/FeTA-iRGD group, where tumor growth was halted after treatment, with one mouse even showing tumor regression (Fig. 5C–H). Digital images and tumor weights on day 30 demonstrated the superior tumor-inhibitory effects of the JQ1@MSN/FeTA-iRGD group (Fig. 5I–J). Furthermore, *Ki67* staining revealed a significant reduction in cell proliferation in the JQ1@MSN/FeTA-iRGD group (Fig. 5K–S13). TUNEL staining indicated markedly enhanced apoptosis in JQ1@MSN/FeTA-iRGD tumor tissues (Fig. 5L–S14). Collectively, these findings highlight the potent *in vivo* antitumor efficacy of JQ1@MSN/FeTA-iRGD.

2.6. JQ1@MSN/FeTA-iRGD-induced ICD triggers potent antitumor immunity

Tumor tissues were collected after treatment to further evaluate whether JQ1@MSN/FeTA-iRGD could induce ICD *in vivo*. Immunohistochemistry revealed significant CRT exposure in tumors treated with JQ1@MSN/FeTA-iRGD (Fig. 6A–E). Subsequently, the immune status of the tumor microenvironment was assessed by quantifying infiltrating immune cells, including $CD11c^+$ DCs, $CD3^+$ T cells and $CD8^+$ T cells. Immunofluorescence analysis demonstrated that JQ1@MSN/FeTA-iRGD significantly increased intratumoral frequencies of $CD11c^+$ DCs, $CD3^+$ T cells, and $CD8^+$ T cells (Fig. 6B–D and F-H). Moreover, the effector molecule Granzyme B in $CD8^+$ T cells was markedly upregulated in the JQ1@MSN/FeTA-iRGD group (Fig. 6D–I).

A vaccination assay was conducted to validate the capacity of JQ1@MSN/FeTA-iRGD to activate antitumor immunity, which is considered the gold standard for assessing ICD *in vivo*. Panc02 cells pretreated with JQ1@MSN/FeTA-iRGD for 24 h were subcutaneously inoculated into the dorsal flanks of C57BL/6 mice as a tumor cell vaccine. 7 days later, mice were challenged with live panc02 cells in the contralateral flank (Fig. 6J). Notably, tumor growth became detectable in control and freeze-thaw groups by day 12 post-implantation. In contrast, the vaccine group exhibited significantly reduced tumor incidence (66 %, 4/6) and delayed tumor progression, suggesting that JQ1@MSN/FeTA-iRGD serves as a potent ICD inducer (Fig. 6K–S15).

Splenocytes were harvested post-experiment to assess long-term immune memory and analyzed for effector memory T cells (TEM) via flow cytometry. The vaccine group showed markedly elevated TEM frequencies in splenocytes, quantified as 1.9-fold and 1.6-fold higher than in the control and freeze-thaw groups (Fig. 6L–N). Collectively, these data demonstrate that JQ1@MSN/FeTA-iRGD activates systemic antitumor immunity through ICD induction, establishing durable immune memory and achieving robust suppression of pancreatic cancer.

2.7. Biosafety evaluation

We performed a biosafety evaluation of JQ1@MSN/FeTA-iRGD to assess its potential for clinical use. Mouse organs were harvested post-treatment and assessed for damage using H&E staining. As shown in Fig. 7A, there were no significant signs of inflammation, tissue damage, or other pathological changes in any of the groups. Liver and kidney functions were analyzed in the treated mice. Fig. 7B–F shows no significant differences in ALT, AST, TBIL, UREA, or CREA levels between the groups. The hemolysis assay results (Fig. 7G) indicated negligible hemolysis of red blood cells at various concentrations of JQ1@MSN/FeTA-iRGD. Collectively, these results confirm the *in vivo* safety of JQ1@MSN/FeTA-iRGD, supporting its potential for safe clinical application.

3. Conclusion

In this study, we have designed a multifunctional nano-platform, JQ1@MSN/FeTA-iRGD, that adopted a triple-mode strategy integrating apoptosis, ferroptosis, and ICD for anti-tumor therapy. This platform enables spatiotemporally controlled drug release, inducing simultaneous apoptosis and ferroptosis while promoting immune-mediated cytotoxicity. It exhibited superior tumor-suppressive effects

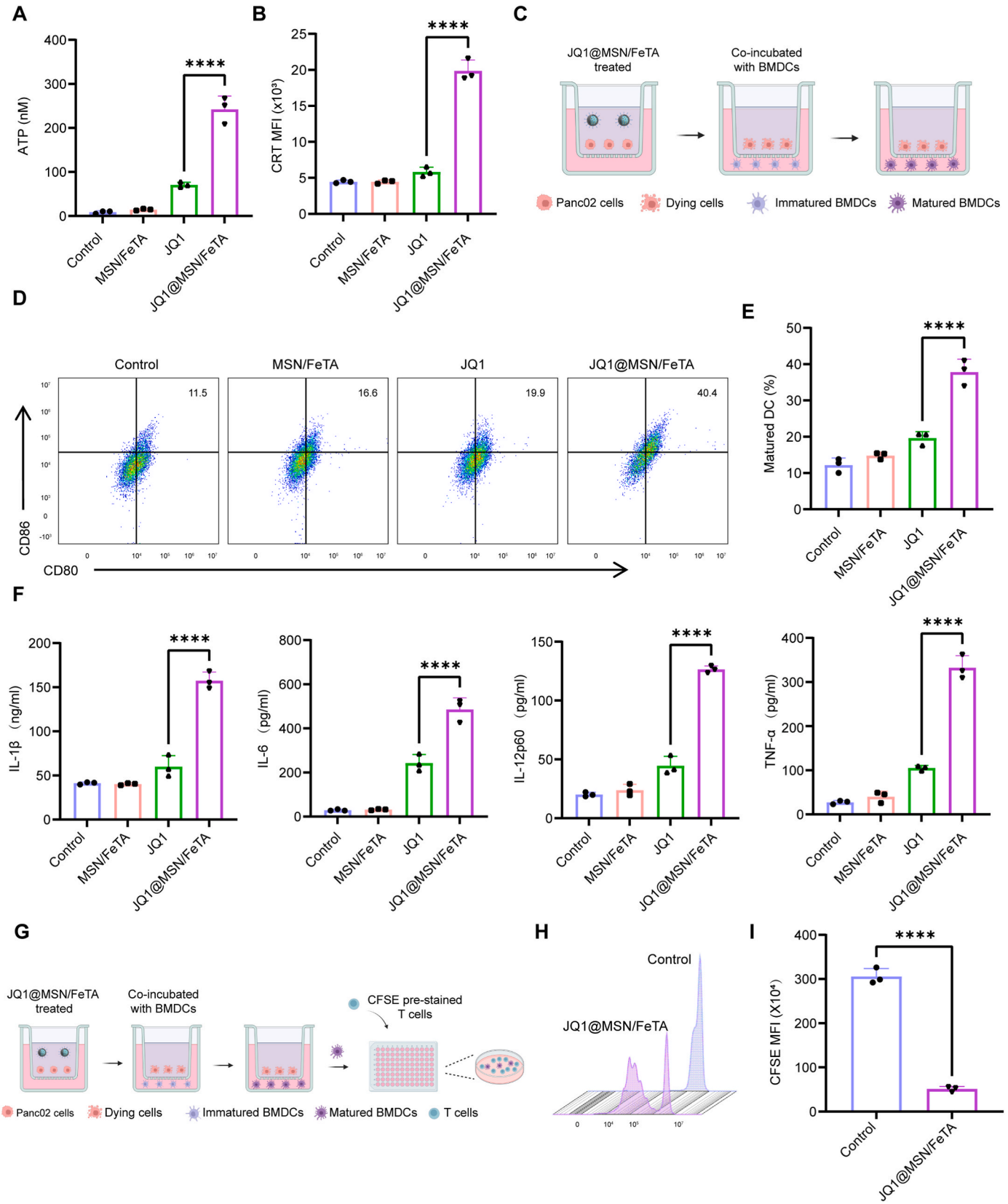

Fig. 3. JQ1@MSN/FeTA promotes DCs maturation via inducing ICD effect *in vitro*. A. Quantitative analysis of ATP in the culture supernatant of Panc02 cells. B. Flow cytometry analysis of CRTexposure on Panc02 cells. C. Schematic diagram of the transwell system detecting the maturation of BMDCs co-cultured with Panc02 cells pre-stimulated with different formulations. D, E. Flow cytometry analysis of BMDCs maturation ($CD80^+$ $CD86^+$). F. Quantitative ELISA analysis of IL-1β, IL-6, IL-12p60, and TNF-α secretion in the supernatant of DCs culture. G. Schematic diagram of the T cell proliferation assay. H, I. Flow cytometry analysis of T cell proliferation stimulated by pre-treated BMDCs.

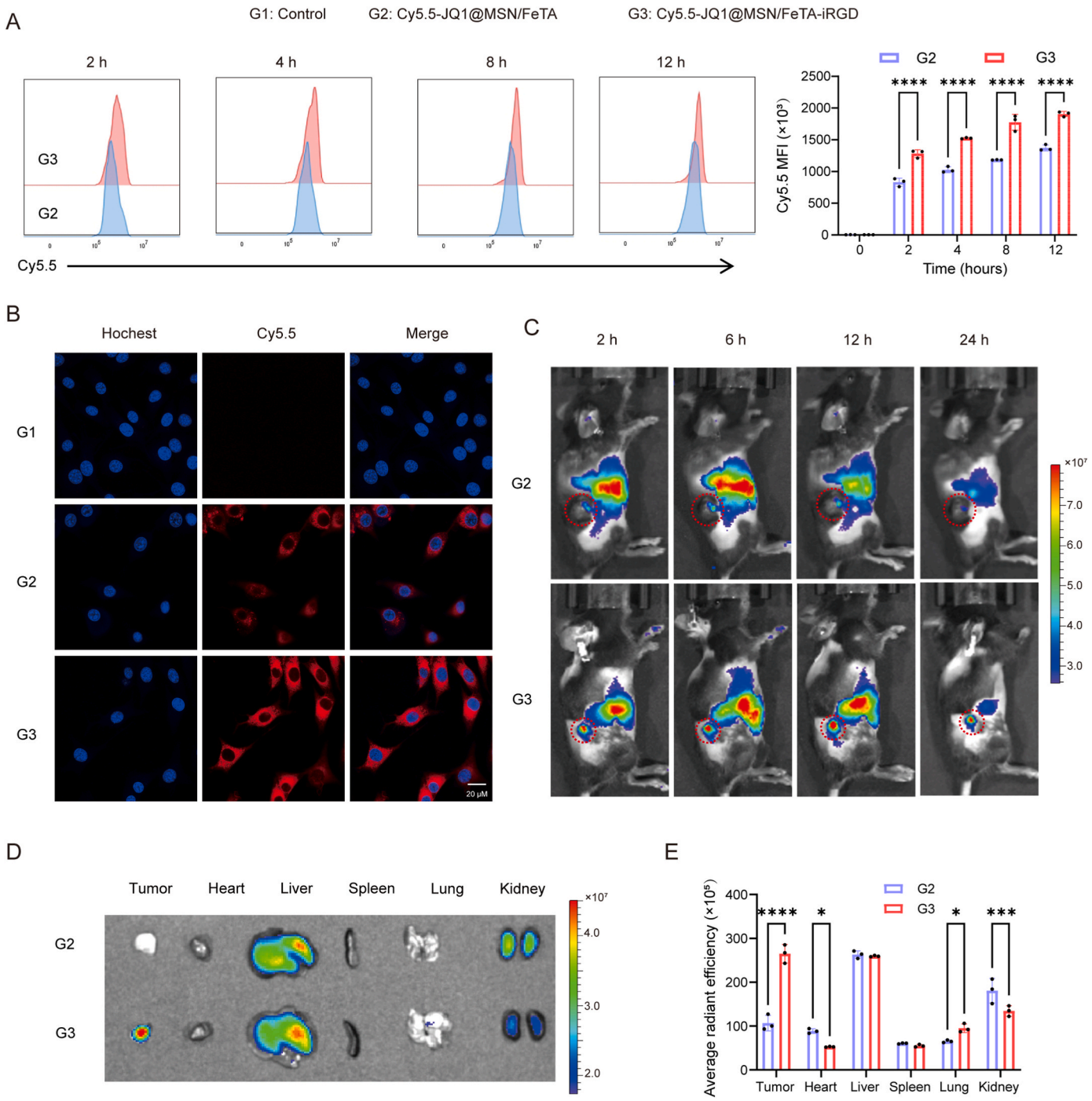

Fig. 4. JQ1@MSN/FeTA-iRGD exhibits excellent tumor-targeting effects. A. Flow cytometry analysis of Panc02 cells uptake of Cy5.5-JQ1@MSN/FeTA (G2) or Cy5.5-JQ1@MSN/FeTA-iRGD (G3). B. Fluorescence imaging of Panc02 cells uptake of Cy5.5-JQ1@MSN/FeTA or Cy5.5-JQ1@MSN/FeTA-iRGD. C. *In vivo* imaging of Panc02 tumor-bearing nude mice after intravenous injection of Cy5.5-JQ1@MSN/FeTA or Cy5.5-JQ1@MSN/FeTA-iRGD. D. Ex vivo organ fluorescence imaging and quantitative analysis of Panc02 tumor-bearing nude mice after intravenous injection of JQ1@MSN/FeTA or JQ1@MSN/FeTA-iRGD at 24 h.

in both *in vitro* and *in vivo* models, effectively addressing the therapeutic limitations associated with rapid resistance to JQ1 monotherapy. Overall, our findings provide a safe and efficient alternative strategy for pancreatic cancer treatment.

4. Experimental section

Preparation of MSN. 380 mg of CTAB was dissolved in 25 mL of deionized water. 0.068 mg of TEA was added and stirred at 300 rpm for 20 min. 4.0 mL of TEOS was gradually introduced and aged at 60 °C for 2 h. The obtained mixture was centrifuged and wash three times with acidic ethanol (ethanol: hydrochloric acid = 10:1) and deionized water. The precipitate was then vacuum-dried to obtain MSN.

Loading of JQ1. 20 mg of JQ1 and 10 mg of MSN were first dissolved in 6 mL of deionized water, followed by stirring at 37 °C in darkness for 12 h. Subsequently, 100 μL of TA (20 mg/mL) and 200 μL of $FeCl_2$ (5 mg/mL) were incorporated into the mixture. To adjust the pH, 1 mL of Tris buffer (100 mM, pH 8.5) was introduced. After the reaction, the JQ1@MSN/FeTA complex was collected by centrifugation, washed three times, and dried. Finally, the loading amount of JQ1 was

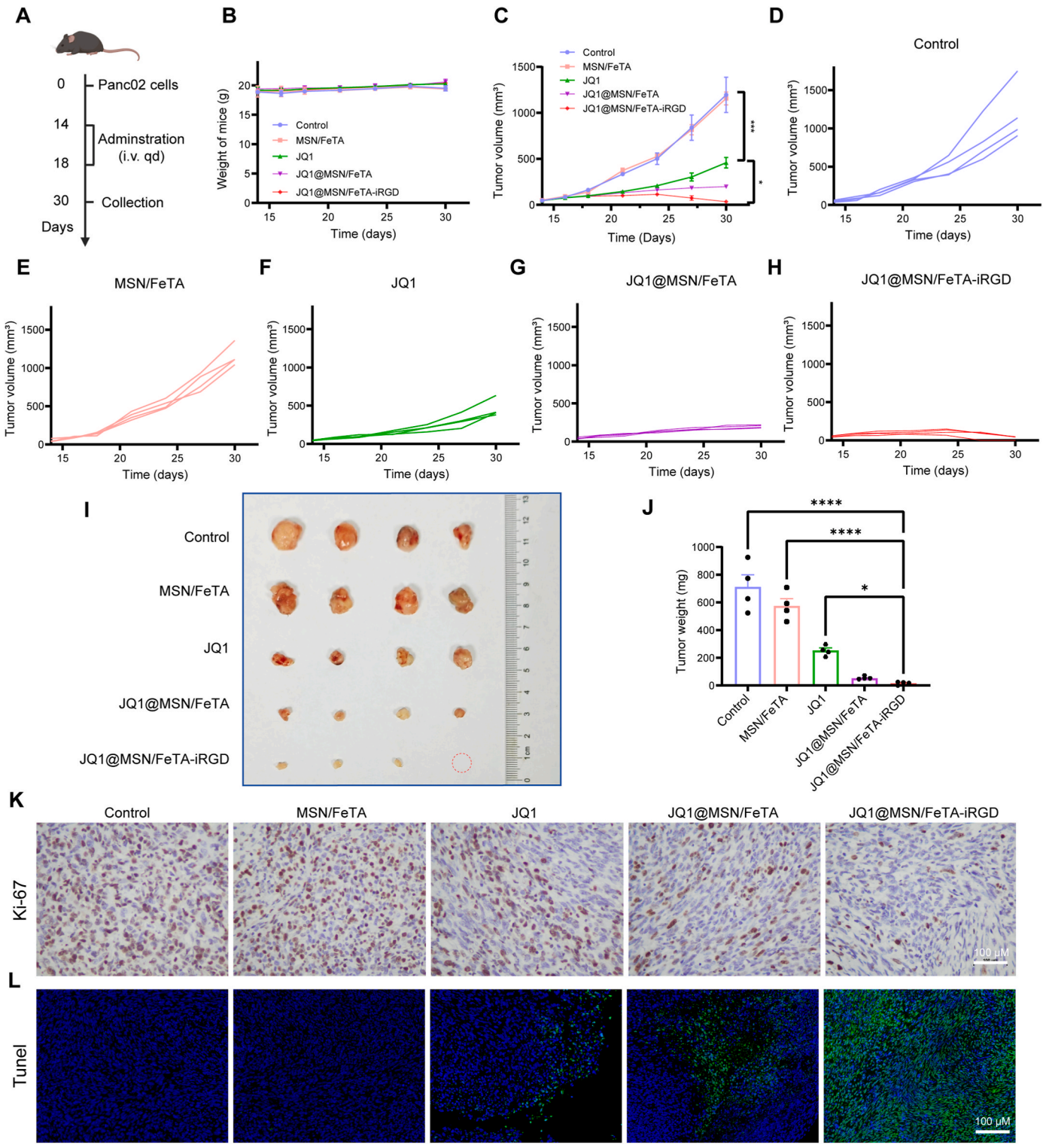

Fig. 5. ***In vivo*** **antitumor effects of JQ1@MSN/FeTA-iRGD.** A. Schedule of the anti-tumor experiment in Panc02 tumor-bearing C57BL/6 mice. B. Body weight of mice in the Control, MSN/FeTA, JQ1, JQ1@MSN/FeTA, and JQ1@MSN/FeTA-iRGD groups during the treatment period. C-H. Tumor volume curves of mice in different groups during the treatment period. I. Tumor photographs of different treatment groups on day 30. J. Tumor weight of the mice. K. Immunohistochemistry images of Ki-67 staining in tumor tissue sections. L. Immunofluorescence images of Tunel staining in tumor tissue sections.

determined using UV–Vis spectrophotometry.

Preparation of JQ1@MSN/FeTA-iRGD. 10 mg of JQ1@MSN/FeTA was resuspended in 20 mL of Tris-HCl buffer (pH 8.5, 10 mM) containing 50 mg of ligands (SH-PEG or SH-PEG-iRGD). The suspension was stirred at room temperature for 6 h. It was then centrifuged, washed with distilled water, and freeze-dried.

In Vitro **Release Study of JQ1@MSN/FeTA-iRGD.** Nanoparticles were dispersed in PBS at various pH levels (7.4, 6.5, 5.5). A total of 5 mL of JQ1@MSN/FeTA (2 mg/mL) was encapsulated in a dialysis bag (MWCO: 3500) and submerged in 45 mL of PBS. The system was stirred at 140 rpm at 37 °C. Every few h, 5 mL of the solution was withdrawn for analysis and replaced with fresh PBS. The concentration of JQ1 was

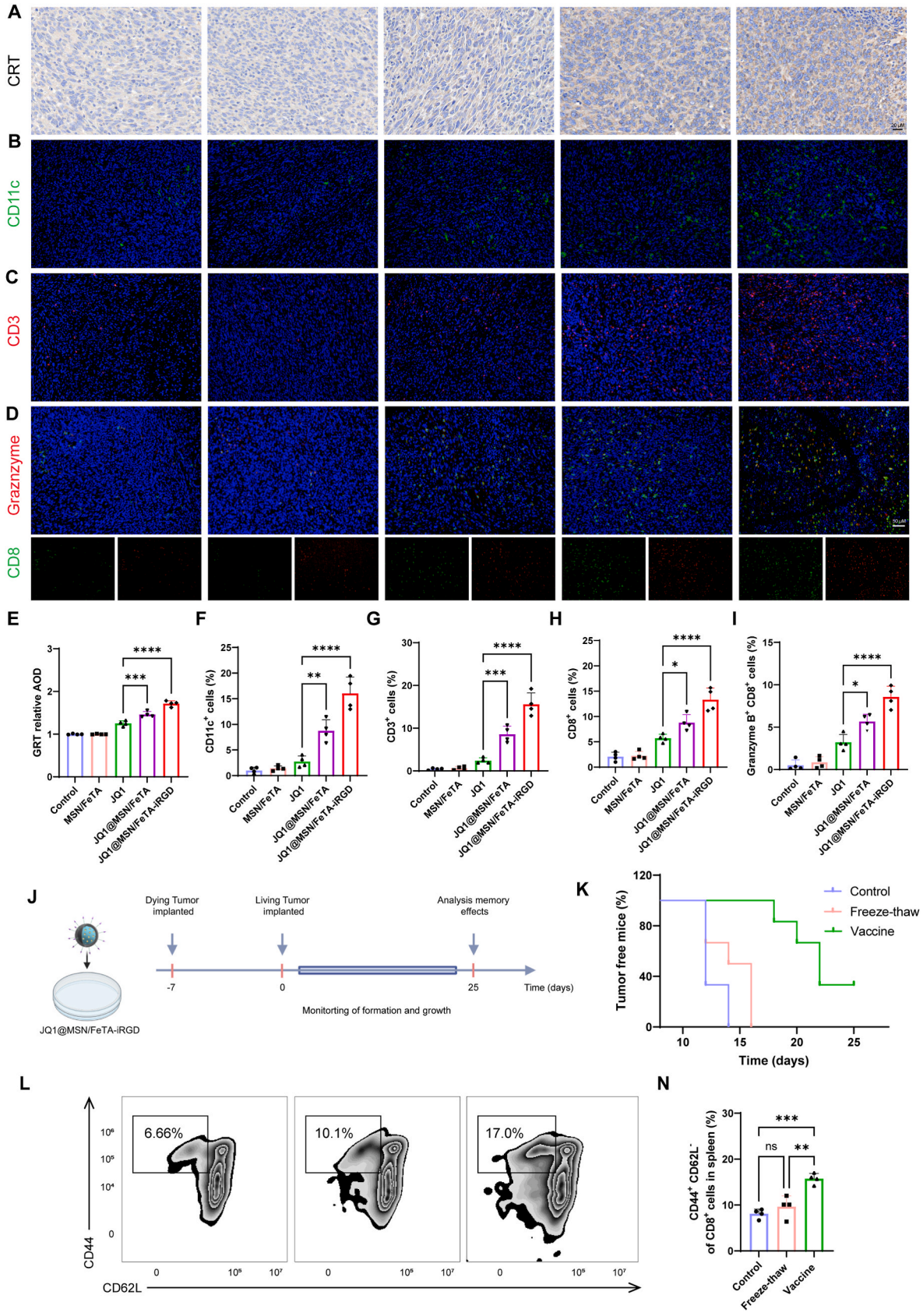

Fig. 6. JQ1@MSN/FeTA-iRGD-induced ICD triggers potent antitumor immunity. A-I. Expression and quantitative analysis of CRT, CD11c^{+} DC, CD3^{+} T cells, CD8^{+} T cells and Gramzyme B^{+} CD8^{+} T cells in tumors (n = 4). J. Flow chart of preventive tumor vaccination. K. Kaplan-Meier survival analysis plot (n = 6). L, N. Flow cytometry profiles and quantitative assessment of TEM in spleens (n = 4).

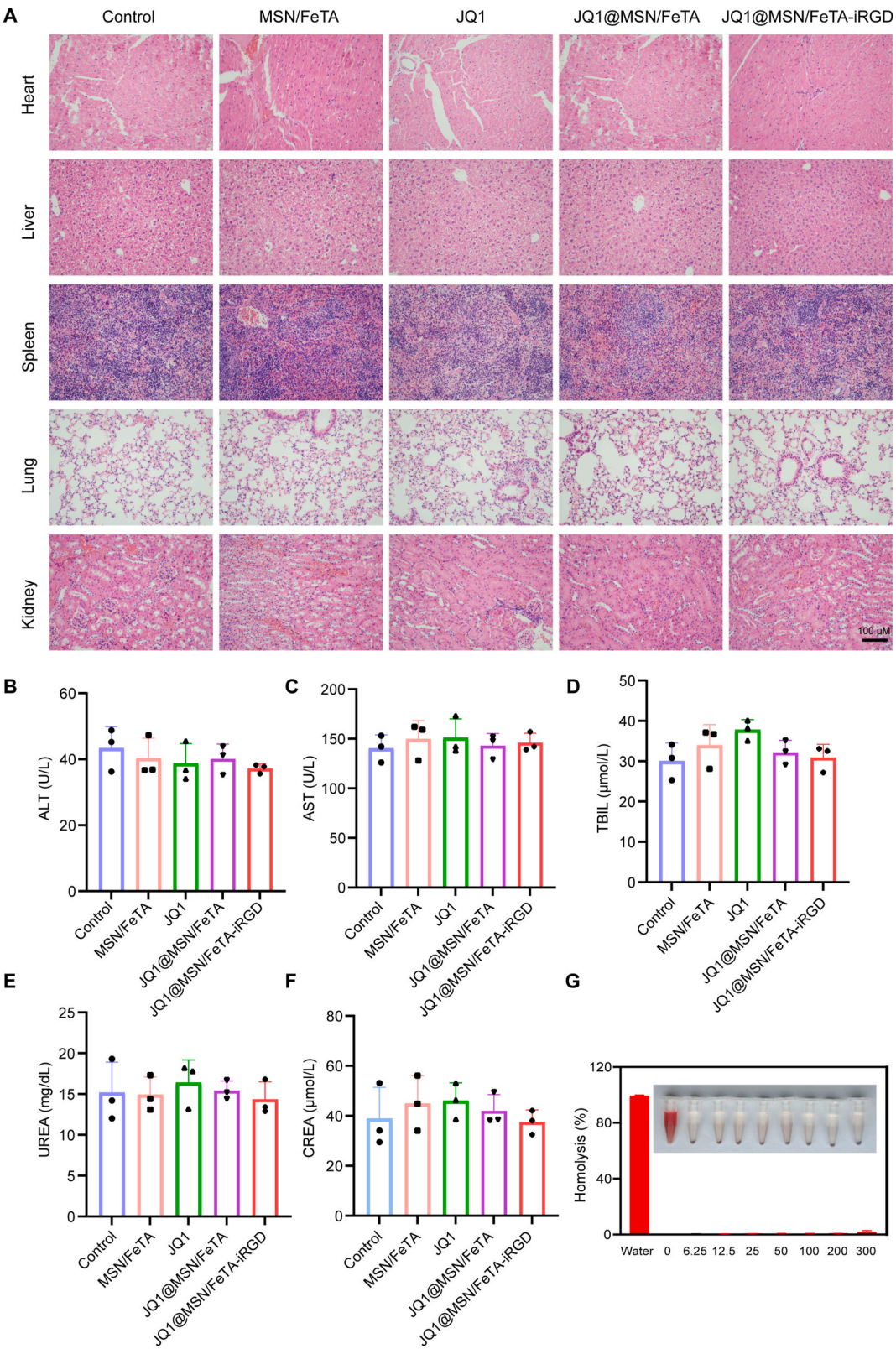

Fig. 7. Biosafety Evaluation. A. HE staining of major organs in mice from different treatment groups. B-F. Serum levels of AST, ALT, TBIL, UREA, and CREA in mice from different treatment groups. G. Hemolysis rate and hemolysis assay imaging.

determined using UV–Vis spectrophotometry, and the release of Fe was assessed via ICP-MS.

Cells and Animals. AsPC-1, Mia-paca-2, Sw1990, Panc-1 and Panc02 cell lines were cultured in DMEM medium supplemented with 10 % fetal bovine serum and incubated at 37 °C in a 5 % CO_2 incubator. Five-week-old female BALB/c mice were purchased from Zhuhai BesTest Bio-Tech Co., Ltd (China) and housed in the Nanhai Animal Laboratory of Sun Yat-sen Memorial Hospital. The mice were maintained in a 12-h

light/dark cycle at 25 °C, and provided unlimited food and water.

***In vitro* cytotoxicity.** The cytotoxicity of the compound was assessed using the CCK-8 assay. First, the experiment involved seeding cells at a density of 5×10^3 cells per well in a 96-well plate, followed by overnight incubation. Fresh culture medium with varying concentrations of the compound was than introduced into each well, then incubated for 24 h. After incubation, added 10 % CCK-8 reagent to each well and then incubated for an additional 2 h. Subsequently, the absorbance was recorded at a 490 nm wavelength using a LabServ K3 microplate reader.

Cell apoptosis assay, ROS generation assays and lipid peroxidation (LPO) detection. Panc02 cells were seeded into well plates and incubated overnight at 37 °C. The cells were then treated with fresh medium containing PBS, MSN/FeTA, JQ1, or JQ1@MSN/FeTA for 12 h.

Apoptosis assay: The cells were harvested and were stained according to the manufacturer's instructions provided with the Annexin V-FITC/PI apoptosis detection kit (Servicebio). The apoptosis rate were then assessed by a flow cytometer (Beckman Cytoflex, USA).

ROS Detection: The cells were incubated with a commercial ROS detection reagent (Beyotime, China) for 1 h, followed with the quantitative expression of ROS by flow cytometry. The image was captured by an inverted fluorescence microscope.

LPO Detection: The cells were incubated with C11 BODIPY (Beyotime, China) for 30 min. Subsequently, the cells were harvested and oxidative state was quantitatively analyzed with flow cytometry.

Mitochondrial Membrane Potential Assays. Panc02 cells were seeded into a well plate and cultured overnight. The cells were then incubated with different compounds for 12 h. Subsequently, the cells were stained with 500 μL of 1 × JC-1 working solution at 37 °C for 20 min and were captured by an inverted fluorescence microscope.

Western Blot Analysis. Samples were lysed in RIPA buffer (Beyotime, China). Proteins were resolved by SDS-PAGE and transferred to polyvinylidene fluoride membrane. Immunoblotting was performed with primary antibodies including anti-GPX4 (Abcam, UK) and anti-GAPDH (ABclonal, China), after which membranes were incubated with HRP-conjugated secondary antibodies (ABclonal, China). Detection was achieved via an enhanced chemiluminescence substrate kit (Thermo Fisher Scientific, USA).

Detection of Extracellular ATP Levels and CRT Expression. After drug treatment, the cell culture supernatant was collected and kept on ice to maintain stability. The extracellular ATP levels in the supernatant were then immediately quantified with an ATP assay kit (Beyotime, China). The cells were collected and resuspended in PBS, followed by a 1-h staining with AF647 anti-mouse CRT. Finally, CRT expression was quantitatively analyzed by flow cytometry.

Maturation of DCs. Bone marrow stem cells were extracted from C57BL/6 mice and cultured in RPMI medium containing IL-4 and GM-CSF for one week to promote differentiation into BMDCs. The immature BMDCs were then seeded into 24-well plates, while Panc02 cells were seeded into transwell inserts. After treating Panc02 cells with different formulations for 12 h, they were co-cultured with BMDCs in the transwell system for 48 h. The BMDCs were stained with PE-labeled anti-mouse CD11c, FITC-labeled anti-mouse CD80, and BV650-labeled anti-mouse CD86 antibodies, and their maturation status was analyzed by flow cytometry. Meanwhile, the culture supernatants were gathered, and the secreted cytokine concentrations were detected using an ELISA kit.

T Cell Proliferation Assay. Using the $CD8^+$ T Cell Isolation Kit (BioLegend), $CD8^+$ T cells were separated from the spleens of 6- to 8-week-old C57BL/6 mice. The $CD8^+$ T cells were stained with 5 μM CFSE for 10 min and then were co-cultured with the mature DCs in low-adhesion 24-well plates at a 5:1 ratio for 3 days. After cultivation, the cells were collected and labeled with AF700 anti-mouse $CD8^+$ antibody for flow cytometry analysis.

***In vivo* Antitumor Therapy.** The antitumor efficacy was assessed in female C57BL/6 mice implanted with Panc02 tumors. Panc02 cells (1×10^6 cells per mouse) were administered subcutaneously into the dorsal region of the mice. After the tumors grew to approximately 50 mm^3,the mice were randomly divided into five groups based on tumor volume (n = 4 per group). The groups were intravenously administered PBS, MSN/FeTA, JQ1, JQ1@MSN/FeTA, or JQ1@MSN/FeTA-iRGD, respectively, for five consecutive days. Tumor volumes (V) were measured and recorded every four days with the equation: $V = a \times b^2/2$, where "a" denotes the tumor's length and "b" its width. After 30 days, tumors were excised, imaged, and their masses were recorded.

***In vivo* Preventive Tumor Vaccination.** Panc02 cells were seeded in 10 cm culture dishes and incubated with JQ1@MSN/FeTA-iRGD for 24 h to induce cell death. Non-specific necrosis was induced via repeated freeze-thaw cycles (dry ice/37 °C water bath) as a control. Subsequently, 1×10^6 dying Panc02 cells or PBS were subcutaneously inoculated into the right dorsal flank of mice. Seven days later, live Panc02 cells (1×10^6 cells/mouse) were injected into the contralateral flank to establish a subcutaneous pancreatic cancer model. Tumor formation and growth were monitored regularly. After 25 days, tumors were excised, imaged, and weighed. Splenocytes were harvested, processed into single-cell suspensions, and analyzed for memory T-cell populations via flow cytometry using APC/Cy7-labeled anti-mouse CD45, FITC-labeled anti-mouse CD3, PC5.5-labeled anti-mouse CD4, AF700-labeled anti-mouse CD8, BV650-labeled anti-mouse CD62L and BV421-labeled anti-mouse CD44 antibodies.

Immunohistochemical Analysis. Tumor tissues and major organs were preserved in 4 % formaldehyde and then embedded in paraffin. Tumor slices were assessed for Ki67 and TUNEL staining, whereas major organs were subjected to H&E staining. In addition, CRT, CD11c, CD3, CD8 and Granzyme B in the tumor sections were detected.

Hemolysis Assay. JQ1@MSN/FeTA-iRGD was incubated with a 2 % (v/v) red blood cell (RBC) suspension at 37 ± 0.5 °C for 3 h. Distilled water acted as the positive control, and normal saline was used as the negative control. Hemoglobin absorbance was measured at 576 nm using a UV–visible spectrophotometer.

Statistical Analysis. Statistical analysis was performed using GraphPad Prism 9 (GraphPad Software). To determine statistical significance, differences between two groups were assessed using the Student's t-test, while comparisons involving multiple groups were analyzed with one-way analysis of variance. Data from *in vitro* experiments are presented as mean ± s.d., while data from *in vivo* experiments are shown as means ± s.e.m. n.s. indicates no significant difference. Asterisks (*) indicate statistically significant differences (*, $p < 0.05$; **, $p < 0.01$; ***, $p < 0.001$; ****, $p < 0.0001$).

CRediT authorship contribution statement

Zhiguo Li: Writing – original draft, Methodology, Conceptualization. **Jinxin Duan:** Writing – original draft, Methodology. **Zhiwen Liu:** Writing – original draft, Methodology. **Weifan Li:** Visualization, Validation, Software. **Yiyin Mai:** Data curation, Formal analysis, Methodology. **Hao Fu:** Conceptualization, Funding acquisition, Resources, Supervision, Validation, Writing – review & editing. **Guotao Yuan:** Writing – review & editing, Supervision, Funding acquisition, Conceptualization. **Jiawei Wang:** Writing – review & editing, Resources, Project administration.

Ethics approval and consent to participate

All the animal experiments were approved by the Institutional Animal Care and Ethics Committee of the Nanhai Animal Laboratory of Sun Yat-sen Memorial Hospital, Foshan, China.The designated animal ethics approval number is AP20230052 and the approved experimental protocol number AEP20230050.

Consent for publication

All authors have read and approved the manuscript.

Funding

This work was supported by the National Natural Science Foundation of China (Grant Nos. 82371856 and 52302359), the Shenzhen Research Funding Program (JCYJ20230807154402004), and the Shenzhen Innovation of Science and Technology Commission (LGKCYLWS2023005), the Guangzhou Science and Technology Projects (Grant No. 2025A03J4278) and the Science and Technology Planning Project of Guangdong Province (Grant No. 2023B1212060013).

Declaration of competing interest

The authors declare that they have no known competing financial interests or personal relationships that could have appeared to influence the work reported in this paper.

Abbreviations:

ATP	adenosine triphosphate
BET	bromodomain and extraterminal domain
DCs	Dendritic Cells
BMDCs	bone marrow-derived dendritic cells
BRD4	bromodomain 4
CRT	calreticulin
DAMPs	damage-associated molecular patterns
H2O2	hydrogen peroxide;
ICD	immunogenic cell death
LPO	lipid peroxidation
MOF	metal-organic-frameworks
MSN	mesoporous silica nanoparticles
RBC	red blood cell; ROS: reactive oxygen species
TA	tannic acid
TEM	transmission electron microscopy
XRD	X-ray diffraction
XPS	X-ray photoelectron spectroscopy
ICP-MS	inductively coupled plasma mass spectrometry

Appendix A. Supplementary data

Supplementary data to this article can be found online at https://doi.org/10.1016/j.mtbio.2025.101696.

Data availability

Data will be made available on request.

References

[1] C.J. Halbrook, C.A. Lyssiotis, M. Pasca Di Magliano, A. Maitra, Pancreatic cancer: Advances and challenges, Cell 186 (2023) 1729–1754, https://doi.org/10.1016/j.cell.2023.02.014.

[2] F. Bray, M. Laversanne, H. Sung, J. Ferlay, R.L. Siegel, I. Soerjomataram, A. Jemal, Global cancer statistics 2022: GLOBOCAN estimates of incidence and mortality worldwide for 36 cancers in 185 countries, Ca-Cancer J. Clin. 74 (2024) 229–263, https://doi.org/10.3322/caac.21834.

[3] L. Rahib, M.R. Wehner, L.M. Matrisian, K.T. Nead, Estimated projection of US cancer incidence and death to 2040, JAMA Netw. Open 4 (2021) e214708, https://doi.org/10.1001/jamanetworkopen.2021.4708.

[4] L. Rahib, B.D. Smith, R. Aizenberg, A.B. Rosenzweig, J.M. Fleshman, L. M. Matrisian, Projecting cancer incidence and deaths to 2030: the unexpected burden of thyroid, liver, and pancreas cancers in the United States, Cancer Res. 74 (2014) 2913–2921, https://doi.org/10.1158/0008-5472.CAN-14-0155.

[5] C. Springfeld, C.R. Ferrone, M.H.G. Katz, P.A. Philip, T.S. Hong, T. Hackert, M. W. Büchler, J. Neoptolemos, Neoadjuvant therapy for pancreatic cancer, Nat. Rev. Clin. Oncol. 20 (2023) 318–337, https://doi.org/10.1038/s41571-023-00746-1.

[6] Z.I. Hu, E.M. O'Reilly, Therapeutic developments in pancreatic cancer, Nat. Rev. Gastroenterol. Hepatol. 21 (2024) 7–24, https://doi.org/10.1038/s41575-023-00840-w.

[7] J.D. Mizrahi, R. Surana, J.W. Valle, R.T. Shroff, Pancreatic cancer, Lancet 395 (2020) 2008–2020, https://doi.org/10.1016/S0140-6736(20)30974-0.

[8] A.G. Cochran, A.R. Conery, R.J. Sims, Bromodomains: a new target class for drug development, Nat. Rev. Drug Discov. 18 (2019) 609–628, https://doi.org/10.1038/s41573-019-0030-7.

[9] M.K. Jang, K. Mochizuki, M. Zhou, H.-S. Jeong, J.N. Brady, K. Ozato, The bromodomain protein Brd4 is a positive regulatory component of P-TEFb and stimulates RNA polymerase II-dependent transcription, Mol. Cell 19 (2005) 523–534, https://doi.org/10.1016/j.molcel.2005.06.027.

[10] Z. Yang, J.H.N. Yik, R. Chen, N. He, M.K. Jang, K. Ozato, Q. Zhou, Recruitment of P-TEFb for stimulation of transcriptional elongation by the bromodomain protein Brd4, Mol. Cell 19 (2005) 535–545, https://doi.org/10.1016/j.molcel.2005.06.029.

[11] A. Dey, A. Nishiyama, T. Karpova, J. McNally, K. Ozato, Brd4 marks select genes on mitotic chromatin and directs postmitotic transcription, Mol. Biol. Cell 20 (2009) 4899–4909, https://doi.org/10.1091/mbc.E09-05-0380.

[12] P. Filippakopoulos, J. Qi, S. Picaud, Y. Shen, W.B. Smith, O. Fedorov, E.M. Morse, T. Keates, T.T. Hickman, I. Felletar, M. Philpott, S. Munro, M.R. McKeown, Y. Wang, A.L. Christie, N. West, M.J. Cameron, B. Schwartz, T.D. Heightman, N. La Thangue, C.A. French, O. Wiest, A.L. Kung, S. Knapp, J.E. Bradner, Selective inhibition of BET bromodomains, Nature 468 (2010) 1067–1073, https://doi.org/10.1038/nature09504.

[13] J.E. Delmore, G.C. Issa, M.E. Lemieux, P.B. Rahl, J. Shi, H.M. Jacobs, E. Kastritis, T. Gilpatrick, R.M. Paranal, J. Qi, M. Chesi, A. Schinzel, M.R. McKeown, T. P. Heffernan, C.R. Vakoc, P.L. Bergsagel, I.M. Ghobrial, P.G. Richardson, R. A. Young, W.C. Hahn, K.C. Anderson, A.L. Kung, J.E. Bradner, C.S. Mitsiades, BET bromodomain inhibition as a therapeutic strategy to target c-myc, Cell 146 (2011) 904–917, https://doi.org/10.1016/j.cell.2011.08.017.

[14] J.A. Mertz, A.R. Conery, B.M. Bryant, P. Sandy, S. Balasubramanian, D.A. Mele, L. Bergeron, R.J. Sims, Targeting MYC dependence in cancer by inhibiting BET bromodomains, Proc. Natl. Acad. Sci. USA. 108 (2011) 16669–16674, https://doi.org/10.1073/pnas.1108190108.

[15] J. Zuber, J. Shi, E. Wang, A.R. Rappaport, H. Herrmann, E.A. Sison, D. Magoon, J. Qi, K. Blatt, M. Wunderlich, M.J. Taylor, C. Johns, A. Chicas, J.C. Mulloy, S. C. Kogan, P. Brown, P. Valent, J.E. Bradner, S.W. Lowe, C.R. Vakoc, RNAi screen identifies Brd4 as a therapeutic target in acute myeloid leukaemia, Nature 478 (2011) 524–528, https://doi.org/10.1038/nature10334.

[16] S. Shu, C.Y. Lin, H.H. He, R.M. Witwicki, D.P. Tabassum, J.M. Roberts, M. Janiszewska, S.J. Huh, Y. Liang, J. Ryan, E. Doherty, H. Mohammed, H. Guo, D. G. Stover, M.B. Ekram, J. Brown, C. D'Santos, I.E. Krop, D. Dillon, M. McKeown, C. Ott, J. Qi, M. Ni, P.K. Rao, M. Duarte, S.-Y. Wu, C.-M. Chiang, L. Anders, R. A. Young, E. Winer, A. Letai, W.T. Barry, J.S. Carroll, H. Long, M. Brown, X.S. Liu, C.A. Meyer, J.E. Bradner, K. Polyak, Response and resistance to BET bromodomain inhibitors in triple negative breast cancer, Nature 529 (2016) 413–417, https://doi.org/10.1038/nature16508.

[17] Bromodomain inhibitors, JQ1 and I-BET 762, as potential therapies for pancreatic cancer, Cancer Lett. 394 (2017) 76–87, https://doi.org/10.1016/j.canlet.2017.02.021.

[18] J. Settleman, Bet on drug resistance, Nature 529 (2016) 289–290, https://doi.org/10.1038/nature16863.

[19] T. Wu, G. Wang, W. Chen, Z. Zhu, Y. Liu, Z. Huang, Y. Huang, P. Du, Y. Yang, C.-Y. Liu, L. Cui, Co-inhibition of BET proteins and NF-κB as a potential therapy for colorectal cancer through synergistic inhibiting MYC and FOXM1 expressions, Cell Death Dis. 9 (2018) 315, https://doi.org/10.1038/s41419-018-0354-y.

[20] A.M. Kurimchak, C. Shelton, K.E. Duncan, K.J. Johnson, J. Brown, S. O'Brien, R. Gabbasov, L.S. Fink, Y. Li, N. Lounsbury, M. Abou-Gharbia, W.E. Childers, D. C. Connolly, J. Chernoff, J.R. Peterson, J.S. Duncan, Resistance to BET bromodomain inhibitors is mediated by kinome reprogramming in ovarian cancer, Cell Rep. 16 (2016) 1273–1286, https://doi.org/10.1016/j.celrep.2016.06.091.

[21] S.J. Dixon, K.M. Lemberg, M.R. Lamprecht, R. Skouta, E.M. Zaitsev, C.E. Gleason, D.N. Patel, A.J. Bauer, A.M. Cantley, W.S. Yang, B. Morrison, B.R. Stockwell, Ferroptosis: an iron-dependent form of nonapoptotic cell death, Cell 149 (2012) 1060–1072, https://doi.org/10.1016/j.cell.2012.03.042.

[22] B. Galy, M. Conrad, M. Muckenthaler, Mechanisms controlling cellular and systemic iron homeostasis, Nat. Rev. Mol. Cell Biol. 25 (2024) 133–155, https://doi.org/10.1038/s41580-023-00648-1.

[23] M. Conrad, D.A. Pratt, The chemical basis of ferroptosis, Nat. Chem. Biol. 15 (2019) 1137–1147, https://doi.org/10.1038/s41589-019-0408-1.

[24] H. Wang, J.S. Fleishman, S. Cheng, W. Wang, F. Wu, Y. Wang, Y. Wang, Epigenetic modification of ferroptosis by non-coding RNAs in cancer drug resistance, Mol. Cancer 23 (2024) 177, https://doi.org/10.1186/s12943-024-02088-7.

[25] J.P. Friedmann Angeli, D.V. Krysko, M. Conrad, Ferroptosis at the crossroads of cancer-acquired drug resistance and immune evasion, Nat. Rev. Cancer 19 (2019) 405–414, https://doi.org/10.1038/s41568-019-0149-1.

[26] I. Efimova, E. Catanzaro, L. Van der Meeren, V.D. Turubanova, H. Hammad, T. A. Mishchenko, M.V. Vedunova, C. Fimognari, C. Bachert, F. Coppieters, S. Lefever, A.G. Skirtach, O. Krysko, D.V. Krysko, Vaccination with early ferroptotic cancer cells induces efficient antitumor immunity, J. Immunotherap. Cancer 8 (2020) e001369, https://doi.org/10.1136/jitc-2020-001369.

[27] J. Zang, X. Wen, R. Lin, X. Zeng, C. Wang, M. Shi, X. Zeng, J. Zhang, X. Wu, X. Zhang, W. Miao, P. Xu, Z. Guo, J. Zhang, X. Chen, Synthesis, preclinical evaluation and radiation dosimetry of a dual targeting PET tracer [^{68} Ga]Ga-FAPI-RGD, Theranostics 12 (2022) 7180–7190, https://doi.org/10.7150/thno.79144.

[28] X. Li, H. Zhong, S. Zheng, J. Mu, N. Yu, S. Guo, Tumor-penetrating iRGD facilitates penetration of poly(floxuridine-ketal)-based nanomedicine for enhanced

pancreatic cancer therapy, J. Contr. Release 369 (2024) 444–457, https://doi.org/10.1016/j.jconrel.2024.04.004.
[29] M.A. Saifi, G. Sathish, M.R. Bazaz, C. Godugu, Exploration of tumor penetrating peptide iRGD as a potential strategy to enhance tumor penetration of cancer nanotherapeutics, Biochim. Biophys. Acta Rev. Canc 1878 (2023) 188895, https://doi.org/10.1016/j.bbcan.2023.188895.
[30] J. Zheng, M. Conrad, The metabolic underpinnings of ferroptosis, Cell Metab. 32 (2020) 920–937, https://doi.org/10.1016/j.cmet.2020.10.011.